HHS Public Access

Author manuscript

Nat Biomed Eng. Author manuscript; available in PMC 2019 December 25.

PET imaging of occult tumours by temporal integration of tumour-acidosis signals from pH-sensitive ^{64}Cu-labelled polymers

Gang Huang[1], **Tian Zhao**[1], **Chensu Wang**[1], **Kien Nham**[2], **Yahong Xiong**[2], **Xiaofei Gao**[3], **Yihui Wang**[3], **Guiyang Hao**[2], **Woo-Ping Ge**[3], **Xiankai Sun**[2], **Baran D. Sumer**[4,*], **Jinming Gao**[1,4,*]

[1]Harold C. Simmons Comprehensive Cancer Center, University of Texas Southwestern Medical Center, 5323 Harry Hines Blvd. Dallas. TX 75390, USA

[2]Department of Radiology, University of Texas Southwestern Medical Center, 5323 Harry Hines Blvd. Dallas. TX 75390, USA

[3]Children's Research Institute, Departments of Pediatrics, Neuroscience, and Neurology & Neurotherapeutics, University of Texas Southwestern Medical Center, 5323 Harry Hines Blvd. Dallas. TX 75390, USA

[4]Department of Otolaryngology, University of Texas Southwestern Medical Center, 5323 Harry Hines Blvd., Dallas, Texas 75390, USA

Abstract

Owing to the diversity of cancer types and to the spatiotemporal heterogeneity of tumour signals, high-resolution imaging of occult malignancy is challenging. ^{18}F-fluorodeoxyglucose (FDG) positron emission tomography (PET) allows for near-universal cancer detection, yet in many clinical scenarios it is hampered by false positives. Here, we report a method for the amplification of imaging contrast in tumours via the temporal integration of the imaging signals triggered by tumour acidosis. The method exploits the catastrophic disassembly, at the acidic pH of the tumour milieu, of pH-sensitive positron-emitting neutral copolymer micelles into polycationic polymers, which are then internalized and retained by the cancer cells. PET imaging of the ^{64}Cu-labelled polymers detected small occult tumours (10–20 mm^3) in the brain, head, neck and breast of mice at much higher contrast than FDG, ^{11}C-methionine and pH-insensitive ^{64}Cu-labelled

*Corresponding authors, jinming.gao@utsouthwestern.edu; baran.sumer@utsouthwestern.edu.

Author Contributions

G. Huang, B.D.S and J.G. are responsible for all phases of the research. G. Huang performed all the experiments and analysis. T.Z. assisted the polymer synthesis and FDG PET imaging, C.W. performed the confocal imaging on cell uptake of nanoprobes. K.N ran the PET/CT scan and imaging analysis. Y.X. did the initial radiolabeling experiments. X.G. and Y.W. prepared the 73C brain tumour model. G. Hao helped with ^{64}Cu coupling with UPS nanoprobes. W.G. assisted in the analysis of the 73C brain tumour study. X.S. helped design FDG and ^{64}Cu PET experiments.

Competing interests

B.D.S. and J.G. are scientific co-founders and scientific advisor of OncoNano Medicine, Inc. G.Huang is scientific advisors for OncoNano Medicine, Inc. T.Z. is currently an employee of OncoNano Medicine, Inc.

Supplementary information is available for this paper at https://doi.org/10.1038/s41551-01X-XXXX-X.

nanoparticles. We also show that the pH-sensitive probes reduce false-positive detection rates in a mouse model of non-cancerous lipopolysaccharide-induced inflammation. This macromolecular strategy for integrating tumour acidosis should enable improved cancer detection, surveillance and staging.

Cancer exhibits diverse genetic and histologic differences from normal tissues[1]. Molecular characterization of these differences is useful to stratify patients towards personalized therapy. However, the strategy may not serve as a broad diagnostic tool because genetic/phenotypic biomarkers are expressed in a subset of patients and significant overlap with normal tissues exist[2, 3]. Deregulated energetics are hallmarks of cancer that occur across many types of cancer[4]. Elevated glucose metabolism in cancer cells has long been associated with aerobic glycolysis, where cancer cells preferentially take up glucose and convert it into lactic acid[5]. More recent studies using ^{13}C-labelled glucose in lung cancer patients further demonstrate accelerated oxidative phosphorylation in addition to glycolysis as a cancer cell mechanism for growth and proliferation[6]. The clinical significance of the glucose metabolism is manifested by the widespread use of ^{18}F-fluorodeoxyglucose (FDG) positron emission tomography (PET)[7] where FDG, a radiolabeled glucose analog, is selectively taken up by overexpressed glucose transporters and trapped inside the cancer cells after phosphorylation by hexokinase for PET detection[8].

Despite broad clinical adoption, FDG has many well-described pitfalls[9–16] including relatively high false rates depending on tumour size and variable levels of FDG uptake in tumours and normal tissues. High physiologic uptake of FDG typically occurs in the brain, heart, kidneys, and urinary tract, obscuring the tumour signal from areas adjacent to these tissues[11]. In head and neck cancer, high FDG uptake in Waldeyer's ring (nasopharyngeal, palatine and lingual tonsils), salivary glands, striated muscle, brown fat, or inflammation/infection all contribute to false positive signals[17, 18]. For tumours less than 1 cm, inadequate accumulation of FDG in tumours over the surrounding normal tissues often leads to false negatives[9, 10, 15, 19]. In addition, skull base tumours in the vicinity of highly metabolic brain parenchyma or oropharyngeal and nasopharyngeal cancers in FDG-avid tonsillar tissue may yield false negative diagnoses[20–23]. The variability of FDG uptake, overlap in retention, and temporal fluctuations in metabolism for both normal and tumour tissues significantly limits the accuracy of FDG PET in cancer detection.

Previously we reported an indocyanine green (ICG)-encoded ultra pH sensitive (UPS) nanoprobe for the broad detection of a wide range of solid cancers by near infrared fluorescence imaging[24]. This optical tracer exploits the phase transition of the polymers to quench and unquench the fluorescence of dyes conjugated to the hydrophobic portion of the polymers. The optical output is discrete, all on or off with no intermediate values, leading to the high specificity and sensitivity in tumour detection. However, it was unclear whether the phase transition behavior of the polymers could be harnessed to generate a response or output other than fluorescence. In the tumour milieu, irreversible capture and integration of polycationic unimers upon pH activation of neutral circulating micelles can lead to increase in polymer dose in acidotic tumours over the surrounding normal tissues. Based on this insight, we hypothesized that the catastrophic phase transition responsible for the binary

fluorescence response could be further exploited to achieve binary tumour specific tissue retention or capture of the activated nanoprobes. Temporal integration of this activated and captured signal can provide signal amplification in only tumours to overcome the spatio-temporal limitations of FDG. To test this hypothesis, we synthesized a positron-emitting radionuclide (^{64}Cu, $t_{1/2}$= 12.7 h)-encoded UPS nanosensor with dual PET and fluorescence functions. PET imaging using ^{64}Cu-UPS showed clear detection of occult malignancy in brain, head and neck, and breast over conventional FDG. Capture of polymers within tumours upon activation represents a second output, in addition to fluorescence, that can be exploited for non-invasive imaging of cancer nodules by PET.

Synthesis of ^{64}Cu-UPS$_{6.9}$ nanosensor

1,4,7-Triazacyclononane-N,N',N"-trisacetic acid (NOTA)- and ICG-conjugated poly(ethylene glycol)-*b*-poly(ethylpropylaminoethyl methacrylate) copolymer (aka UPS$_{6.9}$ for pH transition at 6.9) was synthesized by the atom transfer radical polymerization method (Fig. 1a)[25]. The average numbers of NOTA and ICG per copolymer were determined to be two and one, respectively. After polymer synthesis, ^{64}Cu chelation to NOTA was carried out at 37 °C and pH 6.5 for 15 mins to ensure fully dissociated unimers for efficient copper binding (95%, Fig. 1b). After ^{64}Cu labeling, the solution was brought back to pH 7.4 in sodium carbonate buffer to form micelle nanoparticles (32.7 ± 1.6 nm) (Fig. 1c). Removal of unbound ^{64}CuCl$_2$ and ^{64}Cu-NOTA complex was achieved by centrifugal membrane filtration three times with a molecular weight cutoff of 100 kD. The specific activity of ^{64}Cu-UPS nanosensor is 5.5 mCi/mg (per mass unit) or 165 Ci/mmol for molar activity (~6% NOTA on the UPS polymers were labelled with ^{64}Cu to match the optimal dose for fluorescence imaging). The resulting ^{64}Cu-UPS nanosensor was stable in the mouse serum within 48 hrs by radioactive thin layer chromatography and fluorescence assays (Supplementary Fig. 1). Lowering the pH below the transition pH (6.9) led to micelle dissociation into unimers (8.4 ± 0.2 nm). For comparison, NOTA-conjugated poly(ethylene glycol)-*b*-poly(D,L-lactic acid) (PEG-PLA) nanoparticles with similar size (32.0 ± 2.4 nm) was also synthesized as a non-pH sensitive nanosensor control (Supplementary Fig. 2).

Irreversible activation of ^{64}Cu-UPS$_{6.9}$ in biological milieu

In aqueous saline solution (protein free), UPS$_{6.9}$ copolymers undergo "reversible" micelle assembly/disassembly across a narrow pH span (<0.2 pH, Fig. 2a–b). The protonation process is highly cooperative with a Hill coefficient of 38 (Fig. 2c). Along the pH titration coordinate, nanophase segregation (i.e., micellization) rendered a bistable state solution consisting of highly protonated unimers in solution versus neutral copolymers in micelles (Fig. 2d). This all-or-nothing protonation phenotype without the intermediate states is a hallmark of positive cooperativity[26, 27]. The divergent physical properties of the neutral PEGylated micelles and polycationic unimers account for the molecular basis of capture and integration mechanism in the biological system.

In biological milieu, serum protein binding can "irreversibly" arrest UPS copolymers in the dissociated unimer state upon pH activation of PEGylated micelles (Fig. 3a). We examined the reversibility of the UPS$_{6.9}$ nanoprobes in the presence or absence of 40 mg/ml human

serum albumin (HSA) (Fig. 3b). Results show in the absence of HSA, $UPS_{6.9}$ fluorescence intensity was returning to the base level after pH is reversed from 6.5 to 7.4 multiple times. In contrast, in the presence of HSA, the fluorescence intensity was kept at the On-state after pH reversal. These data suggest that nanoprobe response can be drastically different in the biological environment compared to pristine buffer solutions. This irreversible characteristic contributes to the capture of persistent but fluctuating tumour acidotic signals into stabilized output.

Irreversible capture and uptake of ^{64}Cu-$UPS_{6.9}$ by cancer cells

To investigate whether acidic pH can impact nanoprobe uptake inside cancer cells, we incubated ^{64}Cu-$UPS_{6.9}$ with HN5 head and neck cancer cells in DMEM medium at pH 6.5 and 7.4. To mimic the physiological environment, 40 mg/mL human serum albumin was added in the medium. For comparison, ^{64}Cu-PEG-PLA nanoparticles were used as a non-pH sensitive control. HN5 cells were incubated with the same dose of either nanoparticles (25 μg/mL) for different time periods. Then the radioactive medium was replaced and washed with medium without the tracers. Autoradiography images of HN5 cells from the 96-well plate show pH-dependent uptake of ^{64}Cu-$UPS_{6.9.}$ At pH 6.5, increased amount of positron signals was detected over time, leading to an approximately five-fold increase in cell uptake at 1 h over that at pH 7.4 (Fig. 3c–d, Supplementary Fig. 3–4). Albumin-mediated unimer uptake was investigated by the pretreatment of UPS nanoprobes at pH 6.5 in the presence of HSA and then brought back the pH to 7.4, and was found to correspond to 50% of polymer uptake in HN5 cells at pH 6.5 (Supplementary Fig. 5). HN5 cells incubated with non-pH sensitive ^{64}Cu-PEG-PLA micelles didn't show any observable pH dependence in radioactivity signals, and the cell uptake remained low at both pHs, consistent with the stealth properties of PEGylated micelle nanoparticles[28]. We used laser confocal scanning microscopy to examine the distribution of the $UPS_{6.9}$ (free of ^{64}Cu to avoid radiation exposure) 5 and 60 mins after incubation in albumin-containing medium at pH 6.5. HN5 cells were stained for nucleus, cell membrane and lysosomes by Hoechst (blue), anti-F-actin (cyan) and anti-LAMP1 (green), respectively. Anti-poly (ethylene glycol) antibody was used to label the $UPS_{6.9}$ copolymer. Data show the initial adhesion of the copolymer on the cell surface, followed by internalization inside the HN5 cells at 60 mins. Image overlay shows the internalized $UPS_{6.9}$ punctates colocalized with lysosomes (Fig. 3e).

In vivo capture and integration of ^{64}Cu-$UPS_{6.9}$ in the HN5 tumours

Spatio-temporal characterization of ^{64}Cu-$UPS_{6.9}$ distribution in orthotopic HN5 tumours *in vivo* further validated the capture and integration mechanism. HN5 cancer cells were inoculated in the submental space in the head and neck area of a SCID mouse. After tumours grew to 100–200 mm^3, ^{64}Cu-$UPS_{6.9}$ tracer (0.1 mCi) was injected through the tail vein. At 30 mins, 3 and 24 h, animals were sacrificed and tumours were removed and resected into 30 μm thin slices. Autoradiography analysis showed the initial sporadic capture of ^{64}Cu-$UPS_{6.9}$ in HN5 tumours (mostly at the tumour periphery) at 30 mins and 3 hrs as verified by H&E histology, followed by increased tracer accumulation throughout the whole tumour at 24 h (Supplementary Fig. 6).

^{64}Cu-UPS$_{6.9}$ reduced PET contrast in non-cancerous tissue inflammation over FDG

Non-cancerous tissue inflammation (e.g., infection) frequently causes false positive FDG PET results because inflammatory cells use glucose as a primary source of energy[29]. To compare the imaging response to tissue inflammation by ^{64}Cu-UPS$_{6.9}$ versus FDG, we employed a lipopolysaccharide (LPS)-induced, tumour-free animal model for evaluation. In these experiments, healthy BALB/c mice were used. Two days before PET imaging, LPS was injected subcutaneously into the right hind leg of mice to induce inflammation, while PBS was injected into the left hind leg as control. FDG (150 μCi) and ^{64}Cu-UPS$_{6.9}$ (120 μCi) were intravenously injected and imaged 1 and 24 hrs post-injection, respectively. The FDG signal was significantly higher at the inflammation site with 3.4±0.2 %ID/g, compared to the normal muscle tissue at 0.7±0.2 %ID/g ($P<0.01$, Fig. 4, Supplementary Fig. 7). In contrast, ^{64}Cu-UPS$_{6.9}$ demonstrated slightly higher signal at the LPS-injection site (0.56±0.13 %ID/g) over the control muscle tissue (0.32±0.05 %ID/g), but this difference was not statistically significant. The contrast ratios of inflammation tissue over normal tissue were 4.9±1.3 for FDG versus 1.7±0.5 for ^{64}Cu-UPS$_{6.9}$. The lower contrast ratio by ^{64}Cu-UPS$_{6.9}$ offers a potential advantage to reduce false positive signals from tissue inflammation normally observed in FDG-PET.

^{64}Cu-UPS$_{6.9}$ achieved binary detection of brain tumours

Brain cancer is one of the most lethal forms of cancer without a widely accepted method for early detection[30]. Late diagnosis when symptoms occur often leads to poor prognosis and survival[31]. Conventional metabolic PET tracer FDG cannot be used for brain tumour imaging because of the high physiologic uptake of glucose in the normal brain tissues[32]. To investigate the feasibility of ^{64}Cu-UPS$_{6.9}$ for glioma detection, we utilized an orthotopic glioma mouse model by transplantation of green fluorescent protein (GFP) labeled murine glioma cell line, 73C (astrocytes-derived gliomas with p53$^{-/-}$, PTEN$^{-/-}$, BRAF^{V600E} mutations), into the stratum of mouse brain. At 24 hrs after intravenous administration of ^{64}Cu-UPS$_{6.9}$, PET imaging showed a bright illumination of small sized brain tumours (~10 mm^3) over the dark normal brain tissue background (Fig. 5a, Supplementary Fig. 8). Tissue uptake of ^{64}Cu-UPS$_{6.9}$ was measured at 3.1±1.6 and 0.54±0.3 %ID/g for 73C tumours and normal brain tissues, respectively. The contrast over noise ratio (CNR) was determined to be 15.1±6.8 and the tumour over background ratio (TBR) was 6.0±1.6. For comparison, ^{11}C-methionine (MET), a newly developed amino acid tracer for brain tumour imaging[33–35], was also employed to detect 73C tumours. After i.v. administration, the tissue uptake of MET in tumours was 3.1±0.4 %ID/g at 20 mins. Normal brain tissues had relatively high uptake of MET at 1.9±0.2 %ID/g, lowering the CNR to 2.8±0.7 and TBR to 1.6±0.1 compared to ^{64}Cu-UPS$_{6.9}$ (Supplementary Fig. 9). In the normal brain tissues, blood-brain barrier was effective at keeping the PEGylated micelle form of ^{64}Cu-UPS$_{6.9}$ out of the brain parenchyma. In 73C glioma, tumour acidosis was able to activate ^{64}Cu-UPS$_{6.9}$, leading to significantly increased positron signals. Subsequent investigation of brain tumour slides (8 μm in thickness) by autoradiography and indocyanine green fluorescence correlated microscopically with H&E histology and GFP fluorescence (Fig. 5b). Fluorescence

microscopy data further illustrate that the UPS tracer can cross the blood tumour barrier in 73C gliomas and accumulate not only at the perivascular area but also distribute broadly in the tumour sections (overlay image in Fig. 5c, Supplementary Fig. 10). These data corroborate the feasibility of irreversibly trapping UPS tracers in brain cancer cells to achieve binary tumour imaging outcomes at both macroscopic and microscopic levels.

Non-invasive imaging of multiple tumour types by ^{64}Cu-UPS$_{6.9}$

To investigate the feasibility of ^{64}Cu-UPS$_{6.9}$ to image a broad set of cancers, we evaluated PET imaging of additional head/neck and breast tumour nodules. ^{64}Cu-UPS$_{6.9}$ tracers (0.1 mCi) were injected in the tail vein of tumour-bearing mice. Results show conspicuous detection of occult nodules (10–20 mm^3) in orthotopic HN5 and FaDu head and neck tumours, as well as 4T1 triple negative breast tumours (Fig. 6a, Supplementary Fig. 9–11 for triplicate reports demonstrating robustness of tumour detection). Autoradiography images on another set of tumour models with tumour invasion to the surrounding muscles also showed the increased accumulation of ^{64}Cu-UPS in the tumour tissues over the surrounding normal muscles (Supplementary Fig. 11–13). The tissue uptake were 9.9±2.5, 6.5±2.5 and 5.7±1.2 %ID/g in the HN5, FaDu and 4T1 tumours 18–24 h after i.v. injection of ^{64}Cu-UPS$_{6.9}$ tracers, respectively. The CNRs were 54.3±8.7, 33.5±3.7 and 34.6±12.1 in the HN5, FaDu and 4T1 tumours (n=3 for each tumour type), respectively (Fig. 6b). The TBR values were 21.5±5.6, 16.7±6.0 and 15.6±3.4 in the above three tumour models, respectively. PET imaging using FDG (0.15 mCi) and ^{64}Cu-PEG-PLA (0.12 mCi) in HN5 tumours showed less striking imaging outcomes. In FDG-PET experiments, despite HN5 tumour contrast (5.4±0.7 %ID/g), non-specific uptake of the FDG in brain (7.9±1.6 %ID/g), brown fats (8.1±1.3 %ID/g), tensed muscles (6.3±0.3 %ID/g) created false positive signals that complicated tumour diagnosis (Fig. 6a, c, Supplementary Fig. 14). The high background noise also decreased the CNR value to 1.7±0.6 and TBR value to 2.0±0.5. In the ^{64}Cu-PEG-PLA study, a small percentage (2.0±0.2 %ID/g) of tumour uptake was observed in HN5 tumours 18–24 h after i.v. injection. The CNR and TBR values of ^{64}Cu-PEG-PLA (4.4±1.0 and 3.9±0.4, Fig 6c, Supplementary Fig. 15–16) is significantly lower than ^{64}Cu-UPS$_{6.9}$ (54.3±8.7 and 21.5±5.6, respectively). These results demonstrate that passive targeting through the leaky tumour vasculature is not sufficient to produce high tumour contrast as shown by the low CNR value of conventional ^{64}Cu-PEG-PLA micelle probes. To further demonstrate the effect of tumour acidosis, pretreatment of HN5 tumours with acetazolamide, an inhibitor targeting carbonic anhydrase IX (a tumour acidotic protein) decreased the ^{64}Cu-UPS$_{6.9}$ signals by 30% compared to the PBS control (Supplementary Fig. 17).

Discussion

Biological processes are dynamic and complex with perpetual changes in space and time. The resulting spatio-temporal heterogeneity makes it challenging to accurately diagnose pathologic conditions from normal physiological background. PET or magnetic resonance imaging of acidic tumour microenvironment has been studied extensively in recent years[36–40]. However, conventional pH sensors have low pH resolution in which a 10-fold signal changes occur over 2 pH units[38–41]. Previously we reported an ICG-based ultra-pH sensitive (UPS) nanoprobe for cancer detection by fluorescence imaging[24]. A binary

fluorescent delineation of tumour margins was achieved, which led to accurate cancer surgery and prolonged survival in tumour-bearing mice. The main mechanism was thought to be the coupling of the pH dependent phase transition phenomenon to the quenching and unquenching of the fluorophores conjugated to the hydrophobic segment of the polymers. In this study, we incorporated a ^{64}Cu PET functional moiety in the fluorescent nanoparticle formulation. Unlike the ON/OFF fluorescence reporter, the positron signals are always 'ON' and cannot be quenched, therefore phase transition-based changes in signal analogous to fluorescence were not expected. Contrary to expectation, the positron signal showed a binary pattern of background signal suppression and tumour activation similar to the fluorescence output (Figs. 5–6). While PET imaging overcomes the light penetration limitations of optical imaging, we were curious about the mechanisms for the unpredicted pattern of the positron signal. Clearly, passive accumulation due to EPR effect alone was not sufficient to produce the high tumour contrast, as indicated by the relatively low CNR and TBR values of ^{64}Cu-PEG-PLA compared to ^{64}Cu-UPS in HN5 tumours.

We attribute the dramatically improved sensitivity and specificity of cancer detection by ^{64}Cu-UPS tracers to a "capture and integration" mechanism in the acidotic tumour milieu (Fig. 7). Like most biological signals, tumour acidosis is dynamic with high intratumoural heterogeneity in space and time. Reversible small molecular pH sensors[42, 43] do not show high tumour contrast due to broad pH response leading to background activation and incomplete tumour activation. In addition, their signal output varies with the transient fluctuations in tumour metabolism and pH. Other pH tracers such as pHLIP have been reported to undergo similar capture mechanism by protonation and insertion into cell membrane in the lower pH environment. However, broad pH response and strong binding and insertion to blood cells increased background signals with reduced tumour contrast[40]. Consequently, the tumour-to-muscle ratio is around 8 by pHLIP tracers in LNCaP and PC-3 tumours at 24 hrs post injection[38], compared to >30 fold for HN5 tumours by ^{64}Cu-UPS (Supplementary Table 1). For UPS nanoprobes, binary and irreversible activation below a threshold pH (e.g., 6.9, readily achievable by a diverse set of tumours[44]) can permanently convert the spatio-temporal fluctuations of tumour acidotic signals into stable positron output. The sharpness of the phase transition response in this instance resulted in the specific retention or capture of the ^{64}Cu-bearing polymers in acidic tissues such as tumours, while capture is suppressed in the background normal tissue. More specifically, at different time points (t_1, t_2,… t_n), different regions of the tumour can be acidified below the pH threshold (6.9) as indicated by the green spots in front images (Fig. 7). This transient acidotic signal in turn activates ^{64}Cu-UPS micelles circulating at the tumour site into polycationic unimers, which are irreversibly captured leaving a stable imprint of polymer signal (red spots on positron map). The irreversible capture resulted in increased dose accumulation over time for ^{64}Cu-UPS as validated experimentally (Supplementary Fig. 6). Furthermore, uptake of polymers inside the lysosomes of cancer cells avoids diffusion-caused signal blurring, which may explain the sharp contrast at the tumour and normal tissue boundary even after 24 hrs. Intact micelles are cleared from the tumour sites as well as normal tissues through blood circulation. ^{64}Cu-UPS, by linking the binary activation in response to pH to a novel tissue retention output, suppresses the background while allowing maximal amplification of the tumour signal as approximated by 1 (tumour) or 0 (muscle/brain) outputs.

Data show ^{64}Cu-UPS tracers were able to detect a broad range of occult cancer types (Figs. 5–6) in the brain, head and neck where FDG imaging is obscured by the high signal found in normal brain and tonsil tissues. Moreover, in a non-cancerous, lipopolysaccharide-induced inflammation model, FDG showed significantly increased uptake at LPS-injected muscle site compared to the normal muscle control, whereas ^{64}Cu-UPS tracers showed insignificant elevation (Fig. 4). For tumour imaging, although respectable dose accumulation of FDG was observed in tumours (e.g., 5.4±0.7 %ID/g in HN5 tumours), high physiologic uptake of FDG in healthy tissues hampers cancer-specific detection of tumours. Similar outcome was also observed in small molecular tracer ^{11}C-methionine for brain tumour detection, where high normal brain signals lowered tumour contrast compared to ^{64}Cu-UPS (Fig. 5 and Supplementary Fig. 9). For ^{64}Cu-UPS, coupling the unique binary output of phase transition to capture of the acidotic signal allows a more cancer-specific detection of occult diseases (Fig. 6, see also 3D rotation movies in supplemental videos 1–3). Besides tumour acidosis, other factors such as leaky tumour vasculature, disrupted blood brain barriers (as in the case of 73C glioma), elevated micropinocytosis, and impaired lymphatics may also contribute to the robust contrast of tumours over surrounding normal tissues by ^{64}Cu-UPS. Meanwhile, high uptake of ^{64}Cu-UPS in the reticuloendothelial systems (e.g., liver and spleen) may preclude the use of this agent for the detection of cancers in these organs.

In summary, we report the molecular mechanism of proton transistor-like nanoparticles to capture and integrate tumour acidotic signals into discrete outputs to improve the precision of cancer detection. This represents a second output, tissue retention, coupled to the transistor-like binary behavior of the UPS nanoparticles besides fluorescence readout. The impact of the concept is illustrated by the non-invasive detection of small occult diseases (10–20 mm^3 or 3–4 mm) in the brain, head and neck, and breast by PET imaging. Incorporation of both PET and fluorescence functions in one UPS nanotracer further synergizes two orthogonal imaging modalities, which potentially allow initial whole-body assessment of tumour burden by PET, followed by high resolution fluorescence imaging for local interventions (e.g., biopsy or surgery). We anticipate the proposed chemical integration mechanism will impact early cancer detection and surveillance while creating strategic insights to incorporate molecular cooperativity principles[45] for the design of precision medicine.

Methods

Synthesis of ICG- and NOTA-conjugated UPS$_{6.9}$ nanoprobes and NOTA-PEG-*b*-PLA nanoparticles.

Poly(ethylene glycol)-*b*-poly(ethylpropylaminoethyl methacrylate) (PEG-*b*-PEPA) copolymer was synthesized following the reported procedure using the atom transfer radical polymerization method[24]. The polymers were then dissolved in methanol, ICG-Sulfo-OSu were first added to react with AMA (1:1 molar ratio) through via NHS-ester chemistry[46] for 1 hour. Next, p-SCN-Bn-NOTA were added to react with the remaining AMA (4:1 molar ratio) overnight at room temperature. Unconjugated ICG and NOTA were removed by Millipore ultrafiltration membranes with a molecular weight cutting-off at 10kDa. The

$UPS_{6.9}$ nanoprobes were produced by a solvent evaporation method[47] and concentrated to 5 mg/ml for further usage.

NOTA conjugated PEG-*b*-PLA block copolymer was synthesized by ring-opening polymerization following a published procedure[48]. Briefly, polymerization of D,L-lactide was performed at 110 °C using Fmoc-amine-PEG5K-hydroxyl as the macroinitiator and $Sn(Oct)_2$ as a catalyst. Deprotection of Fmoc was made by 20% piperidine in DMF. After polymer purification with precipitating in ether for three times, the solid polymer was suspended in DMF and react with p-SCN-Bn-NOTA at room temperature overnight. Unconjugated NOTA were removed by Millipore ultrafiltration membranes with a molecular weight cutting-off at 10kDa.

^{64}Cu labeling of $UPS_{6.9}$ or PEG-*b*-PLA nanoprobes.

Chelation of $^{64}Cu^{2+}$ to NOTA on the $UPS_{6.9}$ or PEG-*b*-PLA copolymer was accomplished by adjusting pH to 6.0–6.5 with 4M ammonium acetate buffer for 15 mins at 37 °C. Micelle formation was carried out by adjusting the solution pH to 7.4 by 2M sodium carbonate. Removal of unbound $^{64}CuCl_2$ was achieved by centrifugal membrane filtration with a molecular weight cutoff of 100 kD for three times. The maximum specific activity of ^{64}Cu-UPS nanosensor is 1860 Ci/mmol. Before and after centrifugal filtration, 1 μl of micelle solution was mixed with 8μl DI H_2O and 1μl of 50mM diethylenetriamine pentaacetate (DTPA) for 5 minutes. 2μl mixture was then spotted on a TLC plate, and eluted with the mobile phase (PBS). The labeling efficiency was determined by radio-TLC.

pH titration and dialysis.

$UPS_{6.9}$ polymers was first dissolved in 2.5 ml 0.1M HCl and diluted to 2.0 mg/ml with DI water. Sodium chloride was added to adjust the salt concentration to 150 mM. pH titration was performed by adding small volumes (1 μl in increments) of 4.0M NaOH solution under stirring. The pH increase in the range of 3–11 was monitored as a function of total added volume of NaOH. The fully protonated state and complete deprotonation states (protonation degree equaled 100 and 0%) were determined by the two extreme value points of pH titration curves' 1st derivation. The pH values were measured using a Mettler Toledo pH meter with a microelectrode. Next, $UPS_{6.9}$ polymers with protonation degree at 50% were obtained by adding corresponding volumes of 4.0M NaOH. 10 ml polymer solution was centrifuged using ultra-centrifugation tube with a molecular weight cutting-off at 100 kDa to ~5ml filtrated sample. pH titrations were performed to quantify the amount of polymers and degree of protonation in both residual and filtrate layers. We repeated the experiments three times and data were shown in mean±s.d.

Cell culture.

The cancer cell lines used for *in vivo* tumour models include HN5, FaDu, human head and neck cancers, 4T1 breast cancers, GFP labeled glioma cells with $p53^{-/-}$, $PTEN^{-/-}$ and $BRAF^{V600E}$ mutation (we called it 73C glioma cells). HN5 and FaDu cell lines were obtained from Michael Story's lab; 4T1 were obtained from David Boothman lab; 73C glioma cells was originally obtained from Robert Bachoo lab at UT Southwestern. All cells lines were tested for mycoplasma contamination before use. Negative status for

contamination was verified by Mycoplasma Detection Kit from Biotool. Cells were cultured in DMEM or RPMI with 10% fetal bovine serum and antibiotics.

Animal models.

Animal protocols related to this study were reviewed and approved by the Institutional Animal Care and Use Committee. Female NOD-SCID mice (6–8 weeks, ~20g) were purchased from UT Southwestern Medical Center Breeding Core. For orthotopic head and neck tumours, HN5 and FaDu (2×10^6 per mouse) were injected into the submental triangle area. One week after inoculation, animals with tumour size 20–100 mm^3 were used for imaging studies. Orthotopic murine 4T1 breast tumour model was established in female BALB/C mice (6–8 weeks, ~20g) by injection of 4T1 (5×10^5 per mouse) cells into the mammary fat pads. GFP-transfected 73C murine glioma model was established by implanting 10^4 glioma cells intracranially into the striatum (2mm, 0.5mm, −2.5mm) of the right hemisphere in male C57BL/6J mice (6–8 weeks, ~20g). Gliomas (2–4 mm in diameter) were formed within 2–3 weeks in mice. LPS-induced inflammation animal models were established by subcutaneous injection of 50 μg/ 20 μl LPS into the right hinder leg of BALB/c mice two days before the imaging, 20 μl PBS was injected subcutaneously into the left hinder leg of same mice as control.

Cell uptake assay.

1.5×10^4 HN5 cancer cells were seeded into individual well of 96-well plates (n=3 for each time point) containing 0.2 ml DMEM media for overnight before the nanoprobe incubation. 20 μg/ml ^{64}Cu-$UPS_{6.9}$ or ^{64}Cu-PEG-PLA dispersed in either pH 6.5 or pH 7.4 DMEM medium containing 40 mg/ml human serum albumin were incubated with HN5 cells. At specific time point, the cell wells were washed with cold PBS buffer three times to remove all the non-trapped nanoprobes. Finally the 96-well plates were exposed on Perkin Elmer storage phosphor screens for overnight, then imaged using Typhoon imager for ^{64}Cu tracer quantification. For confocal imaging, after nanoprobe incubation, the cells were fixed with 4% paraformaldehyde in PBS for 10min at RT, and permeabilized with 0.1% Triton X-100 in PBS for 10min at 4 degree. Cells were then stained by Hoechst 33342, Anti-F-Actin and Anti-LAMP1 for nucleus, cell membrane and lysosomes, respectively. Anti-poly(ethylene glycol) antibody was used to label the $UPS_{6.9}$ copolymer.

In vivo PET/CT imaging.

For ^{64}Cu-$UPS_{6.9}$, mouse received ~100 μCi of nanoprobes in 150μL in saline intravenously via tail vein injection, PET/CT images were acquired 18–24 hours post-injection on the Siemens Inveon PET/CT Multi-Modality System for 15 mins. For FDG experiment, mice were fasted for 12 h prior to PET imaging. Each mouse received 150 μCi of FDG in 150 μL in saline intravenously via tail vein injection. PET/CT images were acquired one hour post-injection for 15 mins. The mice were sedated on the imaging bed under 2% isoflurane for the duration of imaging. Immediately after the CT data acquisition that was performed at 80 kV and 500 μA with a focal spot of 58μm, 15-min static PET scans were conducted. The PET images were reconstructed using a Fourier Rebinning and Ordered Subsets Expectation Maximization 3D (OSEM3D) algorithm. Reconstructed CT and PET images were fused and analyzed using Inveon Research Workplace (IRW) software. PET images then were

reconstructed into a single frame using the 3D Ordered Subsets Expectation Maximization (OSEM3D/MAP) algorithm. Regions of interest (ROI) were drawn manually as guided by CT encompassing the tumour in all planes containing the tissue. The target activity was quantitatively calculated as percentage injected dose per gram of tissue (%ID/g). The contrast to noise ratio (CNR) was calculated as[49, 50]:

$$CNR = \frac{Mean\ activity\ (tumor) - Mean\ activity\ (Background)}{SD\ (Background)}$$

The background signal was measured as the mean activity in the surrounding normal muscle tissues with the exception of 73C brain tumours. For 73C glioma, the background signal was measured from the contralateral normal brain tissues. SD (background) was the standard deviation of the background tissues. The tumour to background ratio (TBR) was calculated as Mean activity (tumour)/Mean activity (background).

Ex vivo autoradiography and histology.

Immediately following PET imaging, the mice were sacrificed and tumour and major organs (e.g. brain, liver, spleen, heart, kidney, muscle, etc) were harvested and freezed. Section slides were prepared from each specimen. The slides were first exposed on Perkin Elmer storage phosphor screens, then imaged using Typhoon imager for ^{64}Cu tracer quantification, followed by fluorescence imaging using a LICOR Odyssey flatbed scanner with an 800 nm filter for ICG signal, finally H&E staining were performed for histological correlation of the tumours.

Statistical analysis.

Data are expressed as mean ± s.d. Sample sizes were chosen to ensure adequate power (>85%, at significance of 0.05) to detect predicted effect sizes, which were estimated on the basis of either preliminary data or previous experiences with similar experiments. Differences between groups were assessed by GraphPad Prism 8 using paired or unpaired, two-sided Student’s t-tests for the calculation of P values.

Reporting summary.

Further information on research design is available in the Nature Research Reporting Summary linked to this article.

Data availability.

The authors declare that the main data supporting the results in this study are available within the paper and its Supplementary Information. The raw and analysed datasets generated during the study are available for research purposes from the corresponding authors on reasonable request.

Supplementary Material

Refer to Web version on PubMed Central for supplementary material.

Acknowledgments

We thank R. Bachoo for the original 73C cancer cells, Y. Li and Q. Feng for helpful discussions. This work is supported by the National Institutes of Health (R01CA192221 and R01CA 211930) and Cancer Prevention and Research Institute of Texas (RP180343). Animal imaging work is supported by the UT Southwestern Small Animal Imaging Resource Grant (U24 CA126608) and Radiochemistry and PET imaging by Simmons Cancer Center Support Grant (P30 CA142543), and CPRIT Grant (RP110771) to XS.

References

1. Vogelstein B et al. Cancer genome landscapes. Science 339, 1546–1558 (2013). [PubMed: 23539594]
2. Jacobs TW, Gown AM, Yaziji H, Barnes MJ & Schnitt SJ HER-2/neu protein expression in breast cancer evaluated by immunohistochemistry. A study of interlaboratory agreement. Am. J. Clin. Pathol 113, 251–258 (2000). [PubMed: 10664627]
3. Paik S et al. HER2 and choice of adjuvant chemotherapy for invasive breast cancer: national surgical adjuvant breast and bowel project protocol B-15. J. Natl. Cancer Inst 92, 1991–1998 (2000). [PubMed: 11121461]
4. Hanahan D & Weinberg RA Hallmarks of cancer: the next generation. Cell 144, 646–674 (2011). [PubMed: 21376230]
5. Heiden MGV, Cantley LC & Thompson CB Understanding the Warburg Effect: The Metabolic Requirements of Cell Proliferation. Science 324, 1029–1033 (2009). [PubMed: 19460998]
6. Hensley CT et al. Metabolic Heterogeneity in Human Lung Tumours. Cell 164, 681–694 (2016). [PubMed: 26853473]
7. Zhu A, Lee D & Shim H Metabolic positron emission tomography imaging in cancer detection and therapy response. Semin. Oncol 38, 55–69 (2011). [PubMed: 21362516]
8. Som P et al. A fluorinated glucose analog, 2-fluoro-2-deoxy-D-glucose (F-18): nontoxic tracer for rapid tumour detection. J. Nucl. Med 21, 670–675 (1980). [PubMed: 7391842]
9. Cook GJ, Wegner EA & Fogelman I Pitfalls and artifacts in 18FDG PET and PET/CT oncologic imaging. Semin. Nucl. Med 34, 122–133 (2004). [PubMed: 15031812]
10. Purohit BS et al. FDG-PET/CT pitfalls in oncological head and neck imaging. Insights Imaging 5, 585–602 (2014). [PubMed: 25154759]
11. Truong MT, Viswanathan C, Carter BW, Mawlawi O & Marom EM PET/CT in the thorax: pitfalls. Radiol. Clin. North Am 52, 17–25 (2014). [PubMed: 24267708]
12. Culverwell AD, Scarsbrook AF & Chowdhury FU False-positive uptake on 2-[(1)(8)F]-fluoro-2-deoxy-D-glucose (FDG) positron-emission tomography/computed tomography (PET/CT) in oncological imaging. Clin. Radiol 66, 366–382 (2011). [PubMed: 21356398]
13. Truong MT et al. Integrated positron emission tomography/computed tomography in patients with non-small cell lung cancer: normal variants and pitfalls. J. Comput. Assist. Tomogr 29, 205–209 (2005). [PubMed: 15772538]
14. Bhargava P, Rahman S & Wendt J Atlas of confounding factors in head and neck PET/CT imaging. Clin. Nucl. Med 36, e20–29 (2011). [PubMed: 21467845]
15. Blodgett TM, Mehta AS, Laymon CM, Carney J & Townsend DW PET/CT artifacts. Clin. Imaging 35, 49–63 (2011). [PubMed: 21237418]
16. Fukui MB et al. Combined PET-CT in the head and neck Part 2. Diagnostic uses and pitfalls of oncologic imaging. Radiographics 25, 913–930 (2005). [PubMed: 16009815]
17. Cohade C, Mourtzikos KA & Wahl RL “USA-Fat”: prevalence is related to ambient outdoor temperature-evaluation with 18F-FDG PET/CT. J. Nucl. Med 44, 1267–1270 (2003). [PubMed: 12902417]
18. Perkins AC, Mshelia DS, Symonds ME & Sathekge M Prevalence and pattern of brown adipose tissue distribution of 18F-FDG in patients undergoing PET-CT in a subtropical climatic zone. Nucl. Med. Commun 34, 168–174 (2013). [PubMed: 23196673]

19. Gould MK, Maclean CC, Kuschner WG, Rydzak CE & Owens DK Accuracy of positron emission tomography for diagnosis of pulmonary nodules and mass lesions: a meta-analysis. JAMA 285, 914–924 (2001). [PubMed: 11180735]
20. Harvey RJ et al. PET/CT in the assessment of previously treated skull base malignancies. Head Neck 32, 76–84 (2010). [PubMed: 19536771]
21. Schoder H in Nuclear oncology: pathophysiology and clinical applications. (eds. Strauss HW, Mariani G, Volterrani D & Larson SM) 269–295 (Springer, New York; 2013).
22. Castaigne C, Muylle K & Flamen P in Head and Neck Cancer Imaging. (ed. Hermans R) 329–343 (Springer, Berlin Heidelberg; 2006).
23. schmalfuss I in Head and Neck Cancer Imaging. (ed. Hermans I) 363–385 (Springer, Berlin Heidelberg; 2012).
24. Zhao T et al. A Transistor-like pH Nanoprobe for Tumour Detection and Image-guided Surgery. Nat Biomed Eng 1 (2016).
25. Tsarevsky NV & Matyjaszewski K “Green” atom transfer radical polymerization: from process design to preparation of well-defined environmentally friendly polymeric materials. Chem. Rev 107, 2270–2299 (2007). [PubMed: 17530906]
26. Lopez-Fontal E, Milanesi L & Tomas S Multivalence cooperativity leading to “all-or-nothing” assembly: the case of nucleation-growth in supramolecular polymers. Chemical Science 7, 4468–4475 (2016). [PubMed: 30009001]
27. Williamson JR Cooperativity in macromolecular assembly. Nat. Chem. Biol 4, 458–465 (2008). [PubMed: 18641626]
28. Moghimi SM & Szebeni J Stealth liposomes and long circulating nanoparticles: critical issues in pharmacokinetics, opsonization and protein-binding properties. Prog. Lipid Res 42, 463–478 (2003). [PubMed: 14559067]
29. Hess S, Hansson SH, Pedersen KT, Basu S & Hoilund-Carlsen PF FDG-PET/CT in Infectious and Inflammatory Diseases. PET Clin 9, 497–519 (2014). [PubMed: 26050949]
30. Wen PY & Kesari S Malignant gliomas in adults. N. Engl. J. Med 359, 492–507 (2008). [PubMed: 18669428]
31. Omuro A & DeAngelis LM Glioblastoma and other malignant gliomas: a clinical review. JAMA 310, 1842–1850 (2013). [PubMed: 24193082]
32. Fink JR, Muzi M, Peck M & Krohn KA Multimodality Brain Tumour Imaging: MR Imaging, PET, and PET/MR Imaging. J. Nucl. Med 56, 1554–1561 (2015). [PubMed: 26294301]
33. Becherer A et al. Brain tumour imaging with PET: a comparison between [18F]fluorodopa and [11C]methionine. Eur. J. Nucl. Med. Mol. Imaging 30, 1561–1567 (2003). [PubMed: 14579097]
34. Glaudemans AW et al. Value of 11C-methionine PET in imaging brain tumours and metastases. Eur. J. Nucl. Med. Mol. Imaging 40, 615–635 (2013). [PubMed: 23232505]
35. Juhasz C, Dwivedi S, Kamson DO, Michelhaugh SK & Mittal S Comparison of amino acid positron emission tomographic radiotracers for molecular imaging of primary and metastatic brain tumours. Mol. Imaging 13 (2014).
36. Harris RJ et al. pH-weighted molecular imaging of gliomas using amine chemical exchange saturation transfer MRI. Neuro Oncol 17, 1514–1524 (2015). [PubMed: 26113557]
37. Thews O et al. Activation of P-glycoprotein (Pgp)-mediated drug efflux by extracellular acidosis: in vivo imaging with 68Ga-labelled PET tracer. Eur. J. Nucl. Med. Mol. Imaging 37, 1935–1942 (2010). [PubMed: 20523987]
38. Demoin DW et al. PET Imaging of Extracellular pH in Tumours with (64)Cu- and (18)F-Labeled pHLIP Peptides: A Structure-Activity Optimization Study. Bioconjug. Chem 27, 2014–2023 (2016). [PubMed: 27396694]
39. Vavere AL et al. A novel technology for the imaging of acidic prostate tumours by positron emission tomography. Cancer Res 69, 4510–4516 (2009). [PubMed: 19417132]
40. Weerakkody D et al. Family of pH (low) insertion peptides for tumour targeting. Proc. Natl. Acad. Sci. U. S. A 110, 5834–5839 (2013). [PubMed: 23530249]
41. Urano Y et al. Selective molecular imaging of viable cancer cells with pH-activatable fluorescence probes. Nat. Med 15, 104–109 (2009). [PubMed: 19029979]

42. Gillies RJ, Liu Z & Bhujwalla Z P-31-Mrs Measurements of Extracellular Ph of Tumours Using 3-Aminopropylphosphonate. Am. J. Physiol 267, C195–C203 (1994). [PubMed: 8048479]
43. Gillies RJ, Raghunand N, Garcia-Martin ML & Gatenby RA PH imaging. IEEE Eng. Med. Biol. Mag 23, 57–64 (2004).
44. Volk T, Jahde E, Fortmeyer HP, Glusenkamp KH & Rajewsky MF pH in human tumour xenografts: effect of intravenous administration of glucose. Br. J. Cancer 68, 492–500 (1993). [PubMed: 8353039]
45. Li Y, Wang Y, Huang G & Gao J Cooperativity Principles in Self-Assembled Nanomedicine. Chem. Rev 118, 5359–5391 (2018). [PubMed: 29693377]
46. Ma X et al. Ultra-pH-sensitive nanoprobe library with broad pH tunability and fluorescence emissions. J. Am. Chem. Soc 136, 11085–11092 (2014). [PubMed: 25020134]
47. Wang Y et al. A nanoparticle-based strategy for the imaging of a broad range of tumours by nonlinear amplification of microenvironment signals. Nat. Mater 13, 204–212 (2014). [PubMed: 24317187]
48. Blanco E et al. Beta-lapachone micellar nanotherapeutics for non-small cell lung cancer therapy. Cancer Res 70, 3896–3904 (2010). [PubMed: 20460521]
49. Fin L, Bailly P, Daouk J & Meyer ME A practical way to improve contrast-to-noise ratio and quantitation for statistical-based iterative reconstruction in whole-body PET imaging. Med. Phys 36, 3072–3079 (2009). [PubMed: 19673206]
50. Yan J, Schaefferkoette J, Conti M & Townsend D A method to assess image quality for Low-dose PET: analysis of SNR, CNR, bias and image noise. Cancer Imaging 16, 26 (2016). [PubMed: 27565136]

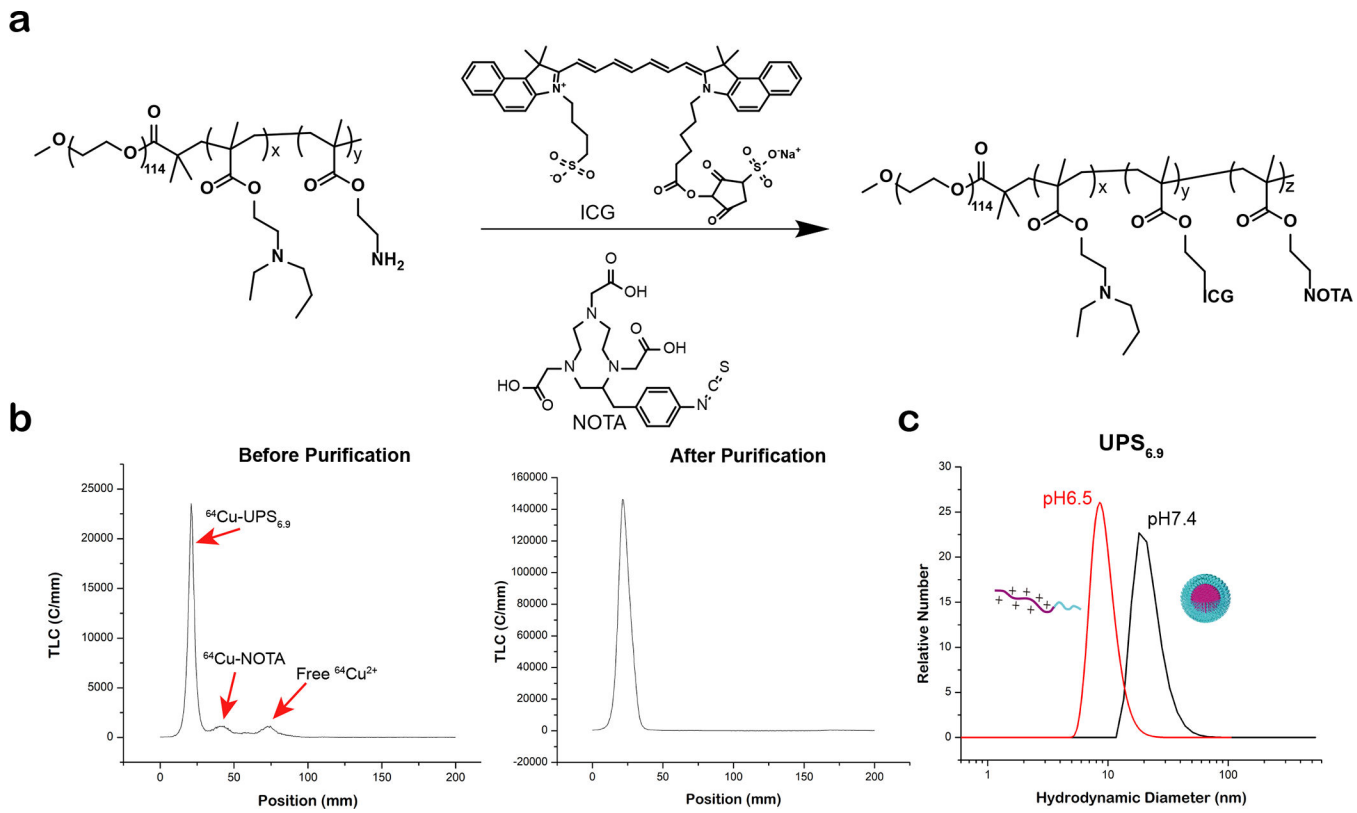

Figure 1 |. Synthesis and characterization of ^{64}Cu-UPS$_{6.9}$ nanoprobes.

a, Schematic syntheses of NOTA- and ICG-conjugated PEG-*b*-PEPA block copolymers. **b,** Radio-TLC chromatogram of ^{64}Cu-UPS$_{6.9}$ nanoprobes before and after centrifugation purification. Labeling efficiency was measured with saline as the developing eluent, and was shown to be more than 95%. **c,** Dynamic light scattering analysis of UPS$_{6.9}$ nanoprobes at pH 7.4 and 6.5 (above and below the pH transition threshold, respectively).

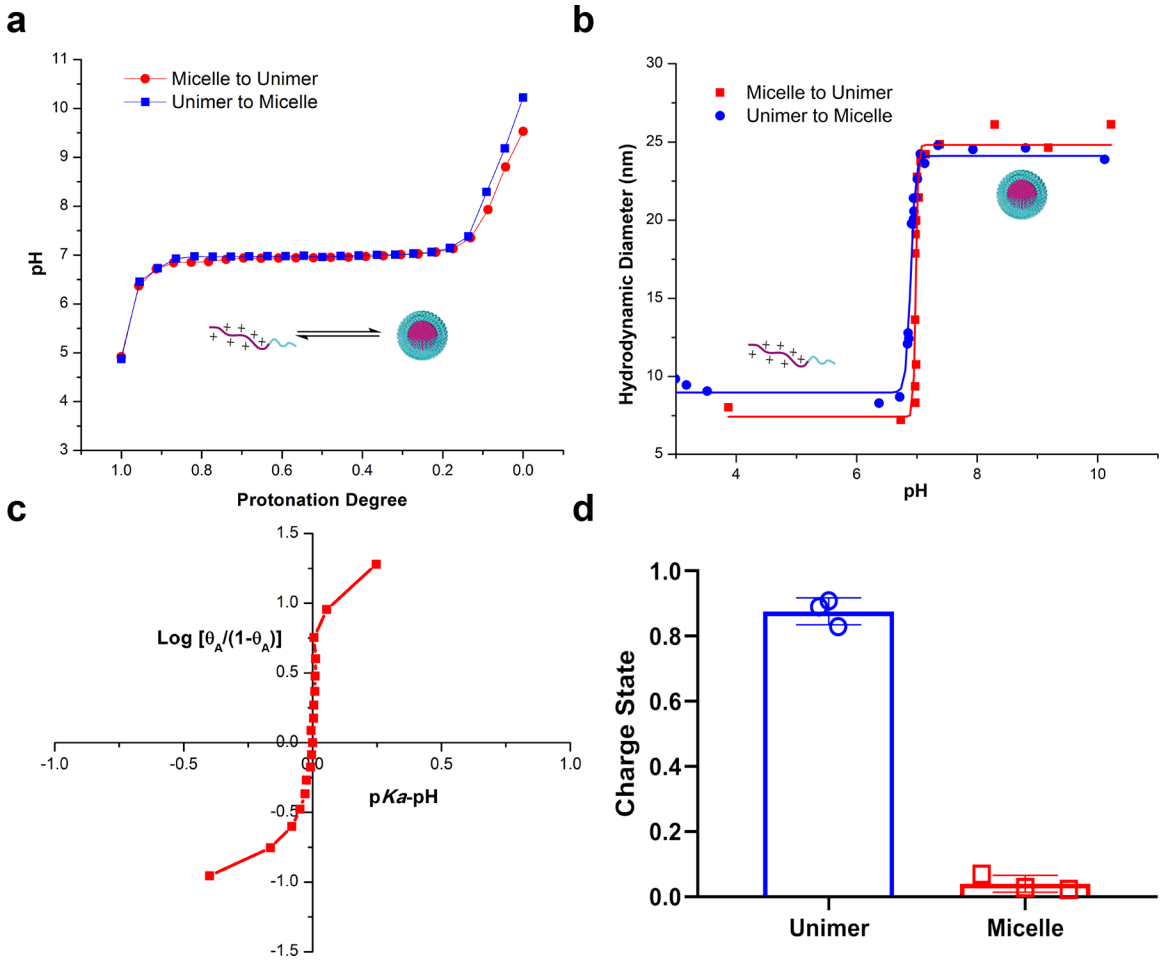

Figure 2 |. All-or-nothing proton distribution of $UPS_{6.9}$ nanoprobes.

a, pH titration curve of $UPS_{6.9}$ showed a reversible and sharp pH transition in saline solution. **b,** Reversible hydrodynamic size change of $UPS_{6.9}$ along the pH titration coordinate. **c,** Quantification of proton binding cooperativity by the UPS copolymers yields a Hill coefficient of 38. **d,** Quantification of unimer and micelle charge states of $UPS_{6.9}$ at an overall protonation degree of 50%. Protons were distributed divergently where unimers were highly charged (~90%) and micelles were almost neutral. Data are presented as individual data points plus mean ±s.d. (n =3), the error bars show the s.d.

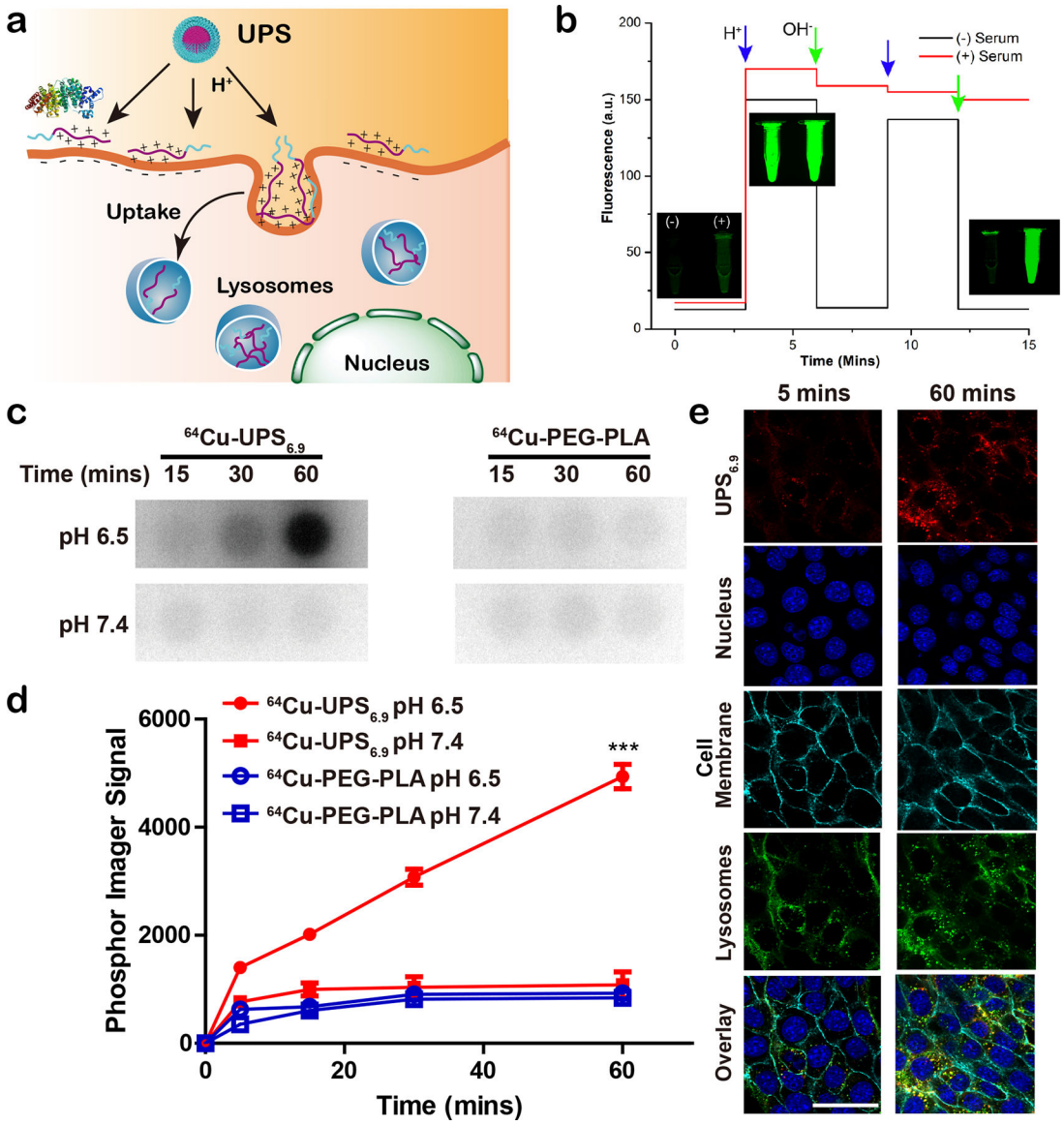

Figure 3 |. Irreversible capture of UPS nanoprobes by serum protein binding and cancer cell uptake after pH activation.

a, Schematic illustration of acid-activated protein binding and membrane adhesion of UPS tracers leading to their sequestration inside lysosomes of cancer cells. **b,** Irreversible arrest of UPS tracers in the unimer state in the presence of serum proteins even after pH reversal to 7.4, compared to the reversible fluorescence changes in the absence of serum proteins. **c,** Autoradiography images of HN5 cells incubated with ^{64}Cu-UPS$_{6.9}$ and ^{64}Cu-PEG-PLA nanoparticles (both at 25 μg/mL) at pH 6.5 and 7.4 over time. **d,** Significantly higher cell uptake of UPS$_{6.9}$ was found at pH 6.5 than 7.4, and over ^{64}Cu-PEG-PLA tracers at both pH. Data are presented as mean ±s.d (n =3); ****P* =0.0003, statistical test made using unpaired two-sided Student's t-test, compared to other groups. The error bars show the s.d. **e,** Confocal microscopy showed UPS$_{6.9}$ were mostly bound to cell membranes at 5 mins, followed by lysosome colocalization at 60 mins after incubation with HN5 cells. Scale bar = 50 μm.

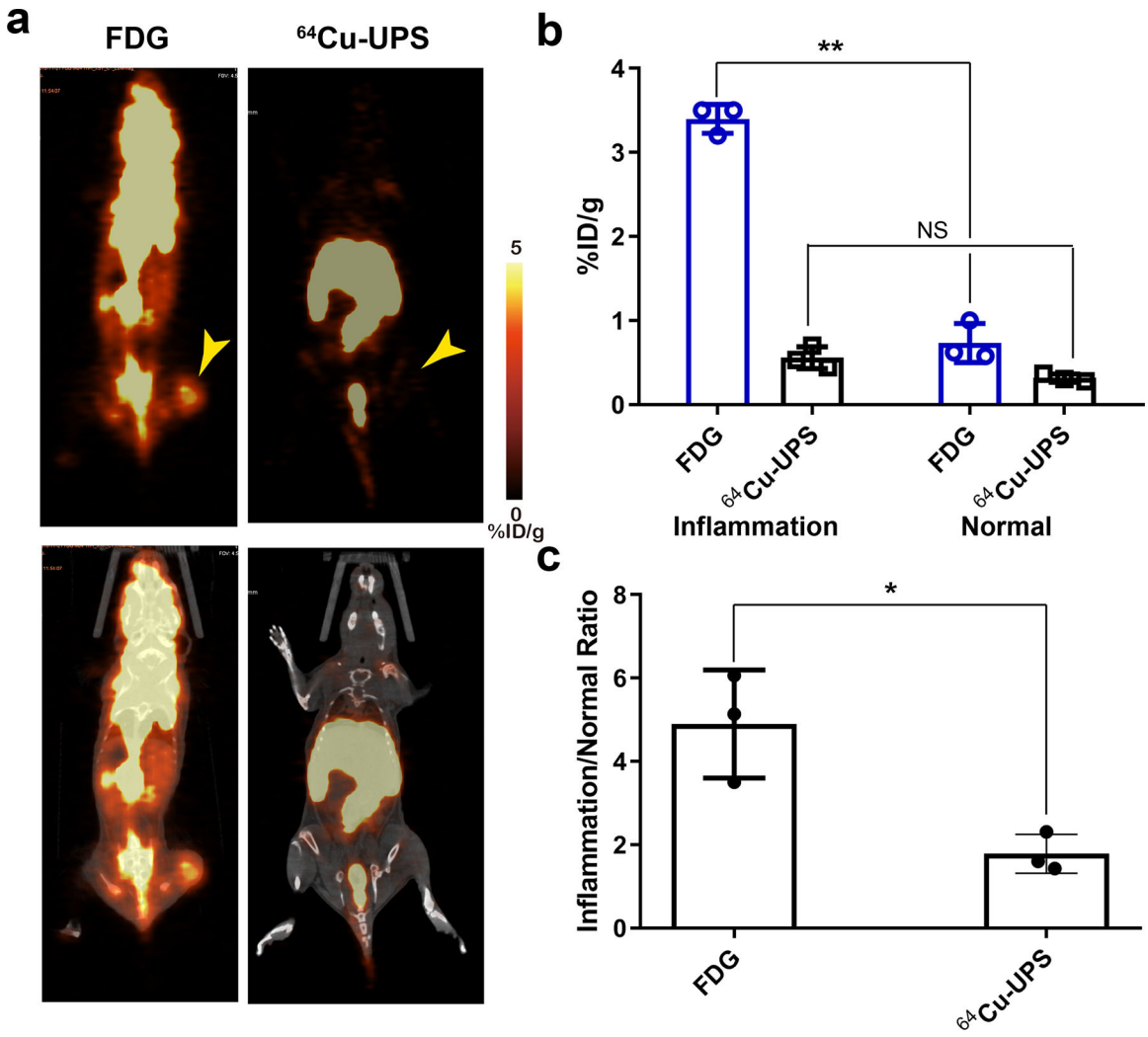

Figure 4 |. ^{64}Cu-UPS$_{6.9}$ reduced false positive PET signals from lipopolysaccharide (LPS)-induced inflammation compared to FDG.

a, PET/CT imaging of BALB/c mice with LPS-injection in the right hind legs by FDG and ^{64}Cu-UPS$_{6.9,}$ respectively. Arrows point to the LPS injection sites in the muscle tissues. Representative images are shown (n=3). **b,** Quantification of PET signals from the inflammation sites and normal left leg muscle tissues by FDG and ^{64}Cu-UPS$_{6.9}$, ** P=0.0024, statistical test made using paired two-sided Student's t-test, NS=not significant. **c,** Inflammation tissue over normal muscle ratios by PET for ^{64}Cu-UPS$_{6.9}$ and FDG. Data are presented as individual data points plus mean ±s.d. (n =3); *P =0.017, statistical test made using unpaired two-sided Student's t-test. The error bars show the s.d.

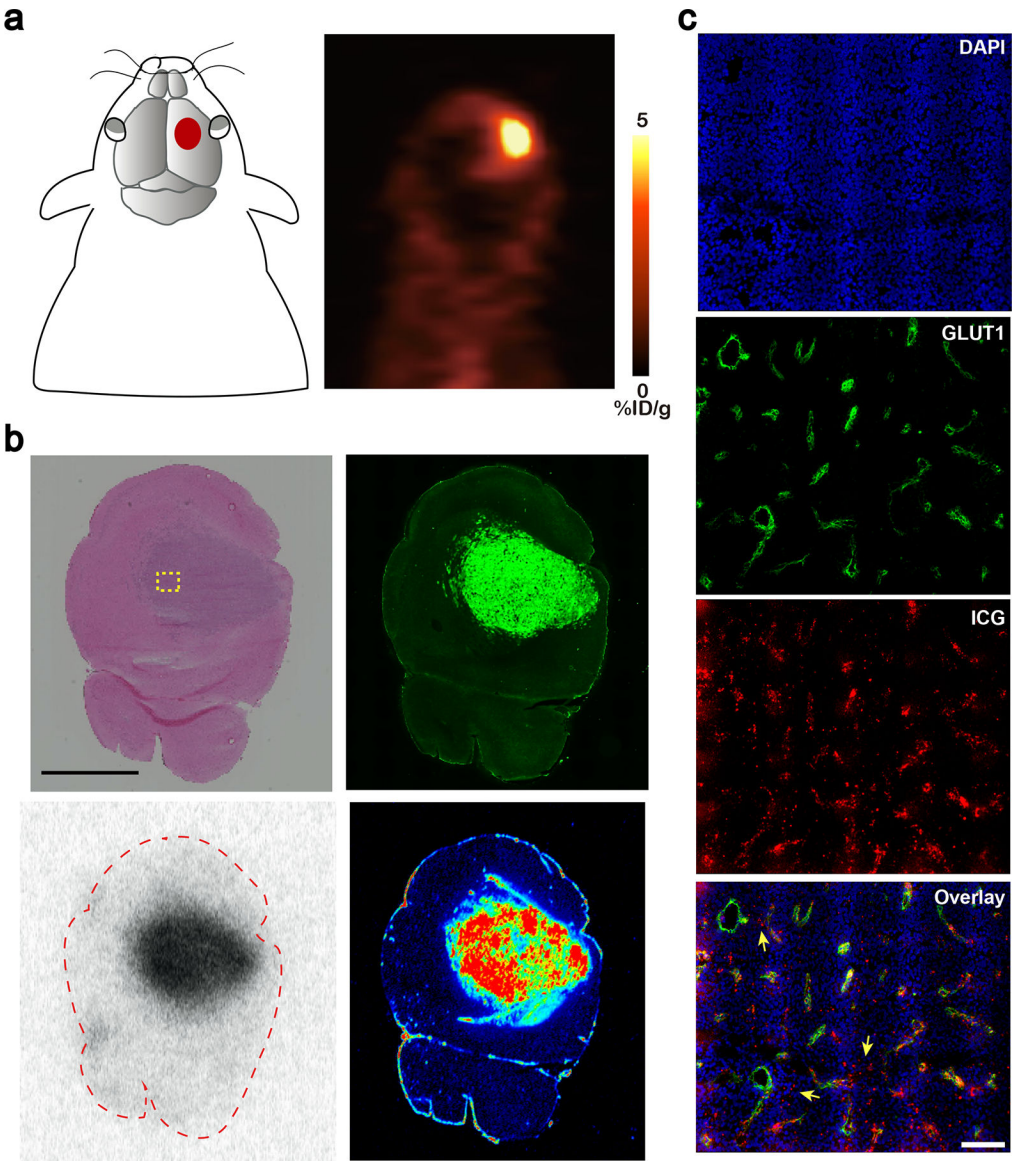

Figure 5 |. The "capture and integration" strategy allowed binary detection of a brain tumour at both macroscopic (animal) and microscopic (subcellular) levels.

a, PET imaging of an orthotopic 73C murine brain tumour in a C57BL/6 mouse by ^{64}Cu-UPS$_{6.9}$. **b,** Correlation of H&E, GFP fluorescence, autoradiography (AR) and ICG fluorescence imaging of brain tumour slide supports the cancer-specific imaging by UPS nanoprobes. Scale bar is 2.5 mm in H&E image and applies to all the images in b. **c,** Fluorescence microscopy analysis of UPS tracer in brain tumours. Correlation of ICG and GLUT1 signals showed that UPS nanoprobes are not only located at the perivascular sites but also distributed throughout the tumours. DAPI: nucleus; GLUT1: vasculature; ICG: UPS nanoprobes, Yellow arrows point to the UPS nanoprobe away from vasculature. Scale bar = 100 μm. Representative images are shown (n=4).

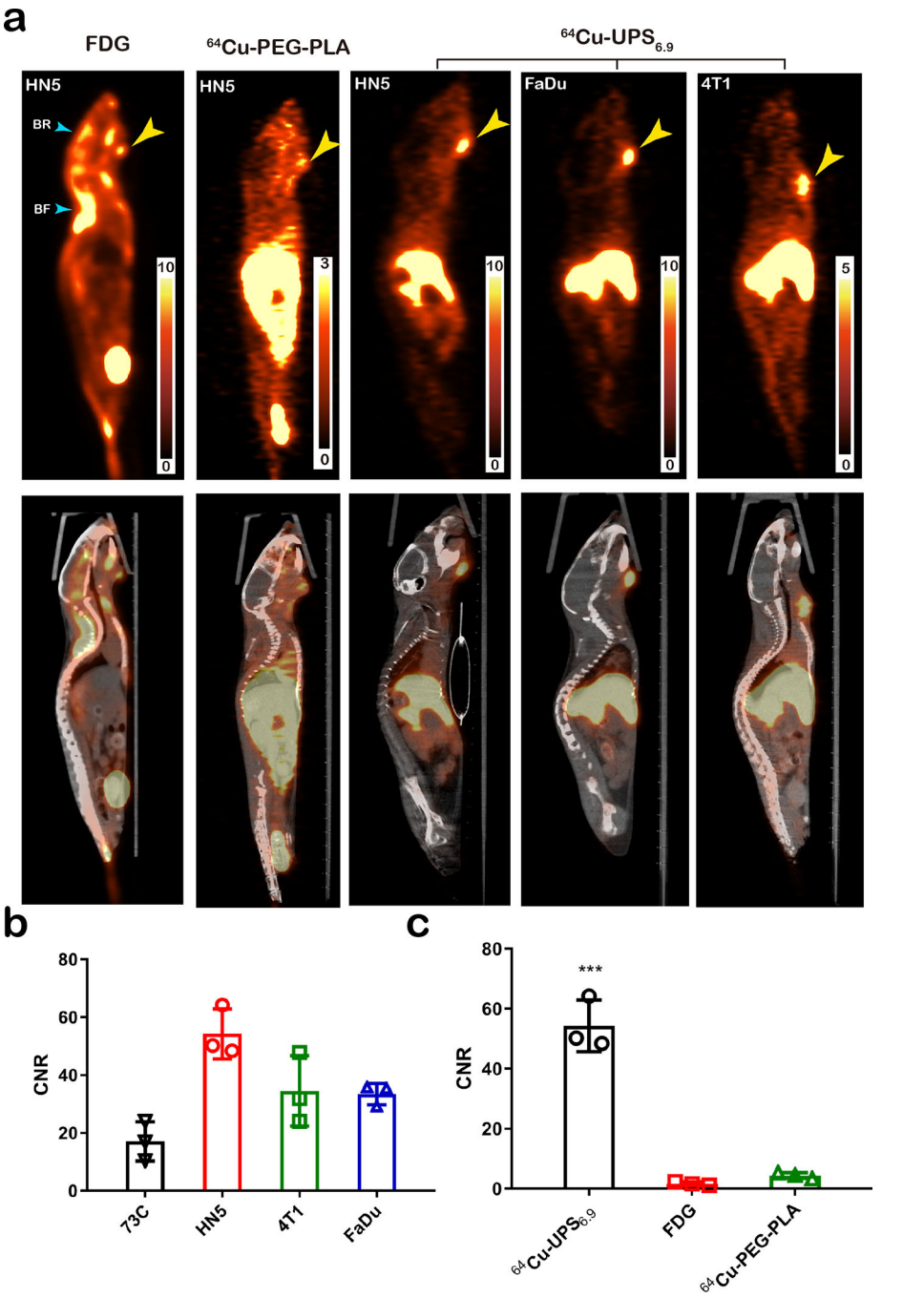

Figure 6 |. Non-invasive digitization of tumour acidotic signals by PET.

a, Cancer-specific detection of various small tumour nodules (10–20 mm^3) by i.v. administered ^{64}Cu-UPS tracers. Orthotopic HN5 and FdDu head and neck cancers and 4T1 triple negative breast cancer were clearly visualized. Representative images are shown (n=3). Scale bar unit: %ID/g. Liver and spleen are the other major organs for UPS uptake. FDG-PET image showed high false rates in the head and neck region (BR, brain; BF, brown fat). **b,** PET quantification of CNR values for ^{64}Cu-$UPS_{6.9}$ in different tumour models. **c,** Comparison of CNR values in HN5 tumours by ^{64}Cu-$UPS_{6.9}$ over FDG and ^{64}Cu-PEG-PLA

nanoparticles. Data are presented as individual data points plus mean ±s.d (n =3); ***P =0.0006, statistical test made using unpaired two-sided Student's t-test, compared to other groups. The error bars show the s.d.

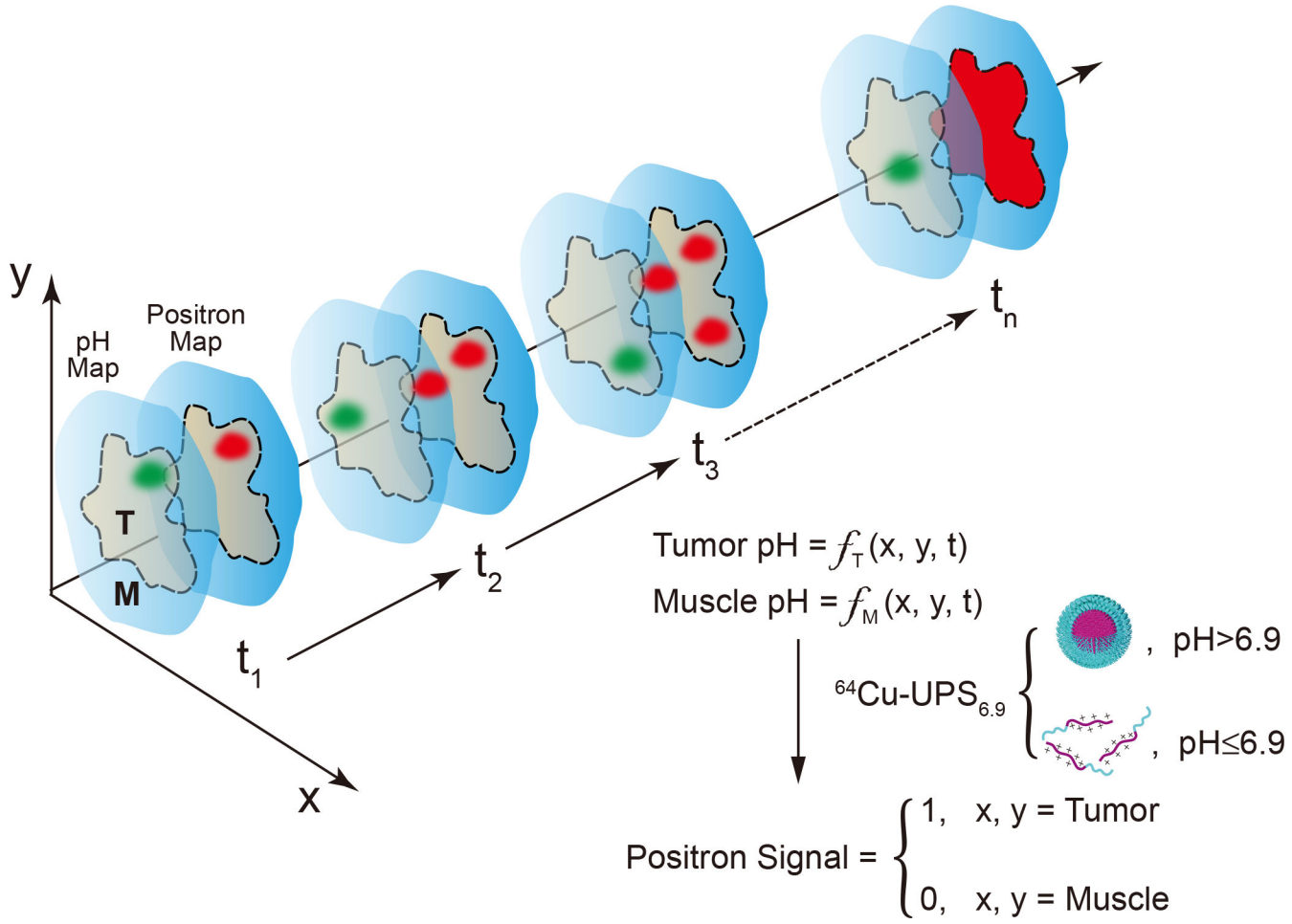

Figure 7 |. Schema for the capture and integration algorithm

converting perpetual spatio-temporal fluctuations in tumour acidosis into step functions of binary response (0 and 1) by the proton transistor sensor. At specific times (t_1, t_2…t_n), different regions of the tumour are acidified below the pH threshold (6.9), indicated by the green spots. The acidic pH signal is permanently captured by ^{64}Cu-UPS$_{6.9}$ as indicated by the red spots on the positron map. Over time, integration of positron signals yields a binary tumour map over normal muscle background. f_T and f_M represent the tissue pH as a function of space and time in the tumour and muscle, respectively.